Excited-state atomic-beam studies of submonolayer adsorption on a fine mesh

G. E. McCown, C. R. Taylor,* and C. A. Kocher
Department of Physics, Oregon State University, Corvallis, Oregon 97331
(Received 4 April 1988)

A surface dipole layer due to adsorbates on a fine mesh can produce localized electric fields capable of ionizing highly excited atoms. This effect is observed when an atomic beam containing high-Rydberg states of Li is incident on a degassed Au mesh having square openings 6 μm across. During the formation of an adlayer on the surface, the adsorbate field is analyzed through measurements of the excited-state atomic-beam flux transmitted through the mesh. The beam-transmission experiments confirm that the excited-state survival probability is surface-layer dependent. Two distinct dips are observed in the transmission as a function of time, during submonolayer adsorption of H_2O and Li on the mesh surface. A cusp between the dips is interpreted as evidence for a change in the sign of the net surface dipole-moment density. These results are compatible with a Langmuir-type model for the survival probability of excited atoms subject to electric-field ionization as they pass through the mesh. Demonstrating that high-Rydberg atoms may be useful as probes for localized electric fields, the experiments serve as feasibility studies for a method of analysis which can readily determine surface dipole orientations and which may have the ability to detect changes in adsorbate coverage at the level of 10^{-4}–10^{-5} monolayer.

I. INTRODUCTION

Atoms or molecules adsorbed on a fine metal mesh can generate short-range electric fields of sufficient magnitude to field-ionize a high-Rydberg state. Using this effect we have developed an atomic-beam technique in which excited atoms serve as probes for the detection and study of surface fields due to adsorbates.

Even at submonolayer coverage, an adlayer present on one side of a mesh can produce a significant electric field within each mesh opening. If the dimensions of the openings are on a scale of microns, fields of hundreds of volts per centimeter can extend over a significant fraction of the open area. As high-Rydberg atoms pass through the mesh, the excited-state survival probability will vary with the adsorbate fields. The mesh transmission, which can be measured during the adsorption process, will decrease during the formation of a net dipole layer on the surface of the mesh.

Previous investigations of atom-surface interactions, with ground-state atomic or molecular beams,[1] including those with a single gross object as the target,[2] are sensitive to atomic arrangements and surface roughness. By contrast, the mesh technique described here, employing highly excited atoms, involves interactions at macroscopic atom-surface distances, of order 10^{-4} cm.

In the experiments to be described, high-Rydberg states of lithium (Li*), with principal quantum numbers near $n=35$ and orbit diameters of order 10^{-5} cm, are produced in an atomic beam. The beam is incident on a gold (Au) mesh target which resembles a foil 2.1×10^{-4} cm thick, with (6.45×10^{-4})-cm square openings. The excited atoms are more comparable in size with the holes and strands of the mesh than with the atoms of the metal lattice. Each Li* atom that emerges from its encounter with the mesh will have passed within 3×10^{-4} cm of the edge of one of the openings. When approaching the mesh surface, an atom in the beam will be affected by the cumulative electric fields from many surface sites. Consequently, the excited atoms are expected to probe average surface properties rather than the effects of individual sites.

An outline of this technique, containing preliminary results from our laboratory, has recently been presented.[3,4] The demonstration experiments are capable of measuring changes in the effective transmission of the mesh due to fractional monolayers of adsorbate. Coverages as low as 10^{-2} monolayer have been detected, and significantly higher sensitivity can probably be achieved.

Here we set forth experimental details, calculations, and further results. Section II gives a brief summary of the relevant properties of highly excited atoms, Sec. III presents calculations of electric fields due to adsorbates, and Sec. IV relates the mesh transmission to the surface dipole density. Recent experiments are discussed in Secs. V–VII. Finally, Sec. VIII includes estimates of the sensitivity that may be attained with this technique.

II. PROPERTIES OF ATOMS IN HIGH-RYDBERG STATES

High-Rydberg atomic states are nearly hydrogenic, with large values of the principal quantum number n, low binding energies, and long radiative lifetimes.[5] Average electron radii increase rapidly with n: $r_n\cong n^2a_0$, where $a_0=\hbar^2/me^2=5.3\times10^{-9}$ cm is the Bohr radius. The electron binding energy is correspondingly low: $W_B\cong e^2/2n^2a_0=13.6\ \text{eV}/n^2$. Thus for $n=35$ the electron radius is $r_n\cong6\times10^{-6}$ cm, and the binding energy is $W_B\cong11$ meV. States with principal quantum numbers as high as $n=290$ have been produced by Rinneberg *et al.*[6]

As the quantum numbers n and l increase, high-Rydberg states become more stable with respect to photon emission. The radiative lifetime of a high-n hydrogenic state varies as n^3 for a fixed low value of the orbital

 ©1988 The American Physical Society

angular momentum quantum number l, and as n^5 for states with $l=l_{\max}=n-1$. In Li most of the states with $n\approx 20$ or higher survive long enough (more than 10^{-4} s) to remain excited in a thermal atomic beam with a flight path of order 30 cm.

A consequence of the weak electron binding is that a highly excited atom can be ionized by relatively low electric fields. An applied field produces oppositely directed forces on the Rydberg electron and the core ion, with ionization occurring when the external force on the electron becomes comparable with the Coulomb force due to the ion. High-Rydberg states are field-ionized by static fields $E_n \lesssim (6\times 10^8$ V/cm)/n^4. For example, Jeys *et al.*[7] found ionization rates above 10^9 s^{-1} for the 34*d* states of Na at threshold fields ranging from 300 to 500 V/cm. Experimentally the detection of high-Rydberg atoms can be accomplished by field ionization as they pass near a charged-particle detector which counts the stripped electrons.

Electric field ionization is the process which allows the high-Rydberg atom to serve as a sensitive probe of localized surface-dipole fields in the vicinity of a fine mesh. The relatively low field-ionization thresholds for these states lead to their ionization at distances from the mesh surface which are typically many times the average spacing between adatoms. For this reason, mesh experiments with excited atoms are relatively insensitive to surface irregularities or roughness, provided that the irregularities have characteristic dimensions which are small relative to those of the mesh. Although the fields in the vicinity of a mesh opening are dipolar and of short range, they typically extend over regions having dimensions much greater than r_n. If a moving atom passes through a static but spatially varying electric field, the atomic state and the maximum value of the field magnitude will determine whether the atom will be field ionized or remain bound.

A highly excited atom can also be ionized as it approaches a metal surface, with the valence electron tunneling into the metal. Surface ionization of a hydrogenic atom near an ideal conducting surface has been treated theoretically by Chaplik[8] and by Janev.[9] As the atom approaches the metal, ionization occurs when the wave function for the valence electron begins to overlap the surface, at a well-defined distance of the same order as the electron radial dimension n^2a_0. In mesh transmission experiments, surface ionization imposes an upper limit on the excited-state transmission.

Fabre *et al.*[10] measured the transmission of high-Rydberg Na atoms through a mesh similar to that used in the present experiments, observing transmission values less than the geometrical transmission (the open fraction of the mesh area). The reduction was found to depend on the principal quantum number n of the Rydberg atom, and is consistent with a model in which the atoms are treated as spheres of radius $\delta\cong 4.5n^2a_0$ which are ionized if they overlap the metal on passage through the slit. The experiment was presented as an investigation of the sizes of excited atomic states, and not as a study of atom-surface interactions. These results are, however, relevant to electric field surface studies undertaken with a fine mesh target, since surface ionization sets a limit on the minimum distance between the Rydberg core ion and the edge of a mesh opening.

III. ELECTRIC FIELDS DUE TO SURFACE DIPOLE LAYERS

If a metal surface is not atomically clean, external electric fields may be present in its vicinity due to surface dipole layers. Polar molecules, for example, may adsorb on the surface with a preferred orientation. Atoms and nonpolar molecules may also become polarized in the presence of the metal surface. In either case, a nonuniform dipole adlayer can generate an electric field in the external region near the surface. This field can be of significant magnitude, as the following calculations will illustrate.

In general, the electric potential V due to a dipole layer on an arbitrary surface S may be written[11]

$$V(\mathbf{r})=-\mu\int_S N(\mathbf{r}')d\Omega(\mathbf{r},\mathbf{r}') \tag{1}$$

in cgs units, where μ is the electric dipole moment of each dipole, N is the surface dipole number density (number of dipoles per unit area), and $d\Omega(\mathbf{r},\mathbf{r}')$ is the solid angle element subtended at $\mathbf{r}$ by the surface element at $\mathbf{r}'$. If N is constant and S is a closed surface, the result is $V=-4\pi N\mu$ for points inside the surface and $V=0$ for points outside, where the sign of μ is taken to be positive when the dipole-moment vectors are directed outward. When a uniform dipole layer is present on a closed surface, this calculation shows that no external electric field is produced. In the experiments to be described, the excited probe atoms will be unaffected by adsorbed layers of equal density on the two sides of a thin mesh sample.

It is worthwhile to examine the electrostatic potentials and fields for surface dipole layers on several mesh-related geometries. In the first case we consider a uniform dipole layer on a semi-infinite plane (the xy plane with $x<0$), which generates a potential

$$V=-2N\mu\phi\ , \tag{2}$$

obtained by integration of Eq. (1) over the half-plane. The angle ϕ is measured clockwise from the negative x axis, so that $\phi=0$ and $\phi=2\pi$ correspond to points just above and just below the dipole plane, accounting for the discontinuity in V noted above. The equipotentials, together with the corresponding field lines, are plotted in Fig. 1.

From this result and the superposition principle one obtains the electric potential due to a uniform dipole layer on an infinitely long strip between $x=-b$ and $x=0$ in the xy plane:

$$V=2N\mu\left[\tan^{-1}\left[\frac{x+b}{z}\right]-\tan^{-1}\left[\frac{x}{z}\right]\right]\ . \tag{3}$$

The electric field components are

$$E_x=2N\mu z\left[\frac{-1}{(x+b)^2+z^2}+\frac{1}{x^2+z^2}\right]\ , \tag{4}$$

$$E_y=0\ , \tag{5}$$

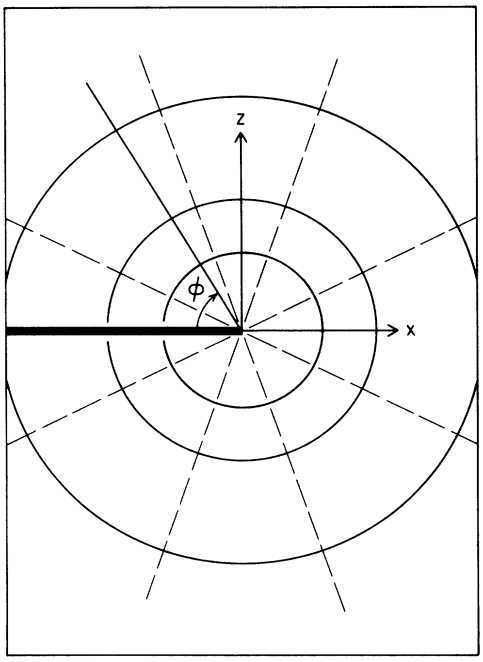

FIG. 1. Semi-infinite plane (heavy line) uniformly covered with oriented dipoles parallel to the z axis, showing equipotentials (dashed) and field lines (solid).

and

$$E_z = 2N\mu \left[\frac{(x+b)}{(x+b)^2+z^2} - \frac{x}{x^2+z^2} \right] . \tag{6}$$

These results are shown graphically in Fig. 2. The magnitude of the electric field is

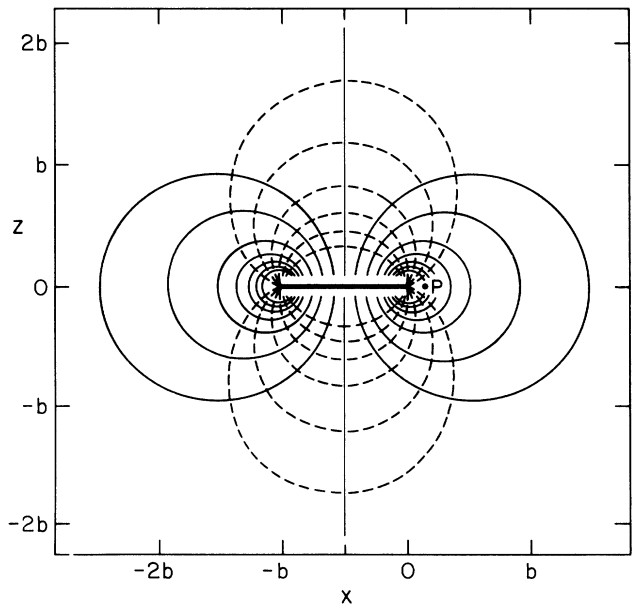

FIG. 2. Equipotentials (dashed) and field lines (solid) near a uniform dipole layer on an infinitely long plane strip. If $N\mu = ea_0 \times 10^{13}$ cm^{-2}, then $E \cong 200$ V/cm at point P.

$$E = \frac{2N\mu b}{\{[(x+b)^2+z^2](x^2+z^2)\}^{1/2}} , \tag{7}$$

which has its maximum in the plane of the dipole strip ($z=0$):

$$E_{\max} = \frac{2N\mu b}{x(x+b)} . \tag{8}$$

For an estimate of the strength of this field, in the context of atomic or molecular adsorption, consider the electric field ionization of atoms with $n \approx 35$, which requires $E \approx 400$ V/cm. To reach this field at $x = b/10$ with $b = 6.45 \times 10^{-4}$ cm (the strand width of the mesh in our experiments), and with dipoles of magnitudes ea_0, would require a surface number density,

$$N = E\frac{x(x+b)}{2ea_0 b} = 1.9 \times 10^{13} \text{ cm}^{-2} . \tag{9}$$

The density of Au atoms on the (100) surface is 1.2×10^{15} cm^{-2}, so the result in Eq. (9) is less than 0.02 monolayer. Since a field of 400 V/cm is sufficient to ionize a typical excited state in the atomic beam, it is clear that surface dipole layer effects will be very important and that submonolayer contributions should be observable in the experiments to be described. If a high-Rydberg atom passing through a hole in the mesh encounters an electric field larger than its field-ionization threshold, it will be ionized and removed from the beam.

If a grounded conducting surface serves as a substrate for the dipole layer, the boundary condition $V=0$ must be satisfied on this surface. Near the edge of an opening, the mesh can be modeled as a conducting region occupying a quadrant, from $\phi = 3\pi/2$ to $\phi = 0$, using the geometry of Fig. 1. If a uniform dipole layer is present on the $\phi = 0$ conducting face, the solution

$$V = \tfrac{4}{3}N\mu(3\pi/2 - \phi) \tag{10}$$

satisfies Laplace's equation in the charge-free region, while also satisfying the boundary condition $V=0$ at $\phi = 3\pi/2$ and the discontinuity condition $\Delta V = 2\pi N\mu$ on the $\phi = 0$ face. The latter condition is appropriate for a dipole layer resulting from a plane charge layer of surface density $\sigma = N\mu/2d$ at a small distance d above the conductor. The image charge plane is then located a distance d below the surface, so that the center of each dipole coincides with the conducting surface. Equations (2) and (10) lead to electric fields having the same configuration, with magnitudes differing by a factor of $\frac{2}{3}$. This factor will be closer to unity for our mesh, which is relatively thin (with thickness $\approx b/3$), so that the presence of a conducting substrate does not seriously modify the results obtained for dipole layers in the absence of a conducting substrate.

A boundary-value solution is given in Appendix A for an infinitely long conducting cylinder of radius a, covered by a nonuniform dipole layer of density $N = N_0 \cos\psi$ on one side ($-\pi/2 < \psi < \pi/2$). Such a distribution corresponds to an adsorbed layer deposited from one side of the cylinder. The potential and field, plotted in Fig. 3, are rather similar in configuration to those for the plane strip of Fig. 2. If $b \approx a$, the fields at corresponding dis-

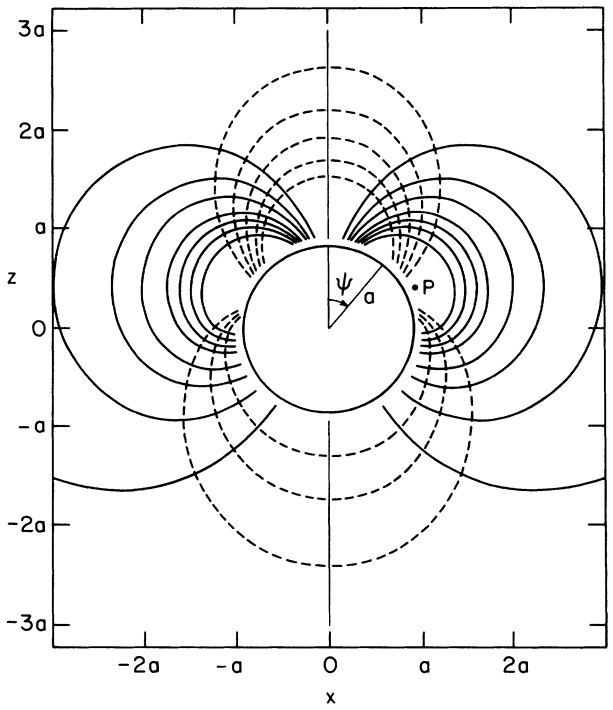

FIG. 3. Equipotentials (dashed) and field lines (solid) due to a dipole layer of surface density $N=N_0\cos\psi$ on the upper half of an infinitely long conducting cylinder. If $N_0\mu=ea_0\times10^{13}$ cm^{-2}, then $E\cong200$ V/cm at P.

tant points are also of comparable magnitude and direction, suggesting that simple plane-strip calculations (as in Fig. 2) provide a reasonably good means of determining the localized electric field due to an adsorbed layer on one strand of a mesh substrate. More distant strands, beyond those bounding a given opening, have only a small effect.

In Appendix B the potential is calculated for a uniform dipole layer on a plane rectangular patch. From a superposition of square patches the potential and the field can be obtained for a plane mesh with square openings. Constant-field contours showing E_z for a single square opening in an infinite dipole plane are plotted in Figs. 4 and 5, where Fig. 5 shows one-quarter of the mesh opening. At the center of the opening the field magnitude is given by Eq. (B6): $E_c=8\sqrt{2}N\mu/b$. This result is approximately equal to the result from Eq. (8) with $x=b/2$, multiplied by 4 (for four strips bounding the opening).

All of the field configurations discussed here are dipolar in character, with field lines forming loops in the free-space region exterior to the dipole layer. Compared with fields due to net charges, dipolar fields fall off more rapidly with distance. The difficulty of measuring such fields by traditional means is evident from calculations for the deflection of a charged particle moving through them. Appendix C contains calculations of the trajectory for a slow electron or ion moving parallel to the z axis, past the edge of a uniform dipole layer on a semi-infinite plane strip. This calculation, which uses the field components given in Eqs. (4)–(6), leads to the following result for the angular deflection α:

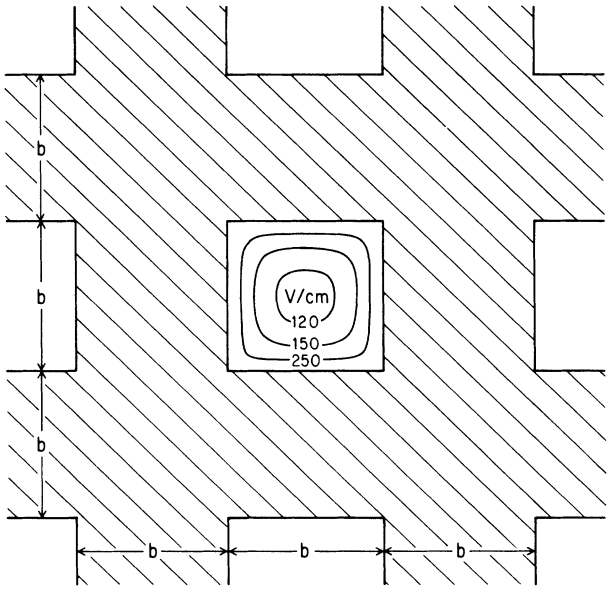

FIG. 4. Contours of equal field magnitude inside a square opening in a plane mesh covered uniformly with oriented dipoles. The fields shown are produced by a dipole density $N\mu=ea_0\times10^{13}$ cm^{-2} with $b=6.45$ μm.

$$\alpha=2\pi\left[\frac{2qN\mu}{mv_0^2}\right]^2\ln\left[\frac{(2x_0+b)^2}{4x_0(x_0+b)}\right], \tag{11}$$

where q and m are the charge and mass, respectively, of the particle, and x_0 is the distance from its trajectory to the edge of the strip. In this calculation the first-order approximation, proportional to $qN\mu/mv_0^2$, is equal to zero. The result given in Eq. (11) is therefore small because it is of second order in this quantity. For example, if a 1-eV particle with $q=e$ passes at a distance $x_0=b/10$ from the edge of a strip bearing dipoles of magnitude $\mu=ea_0$ at a density $N=1.9\times10^{13}$ cm^{-2}, the predicted deflection is only 1.6×10^{-3} rad. By contrast,

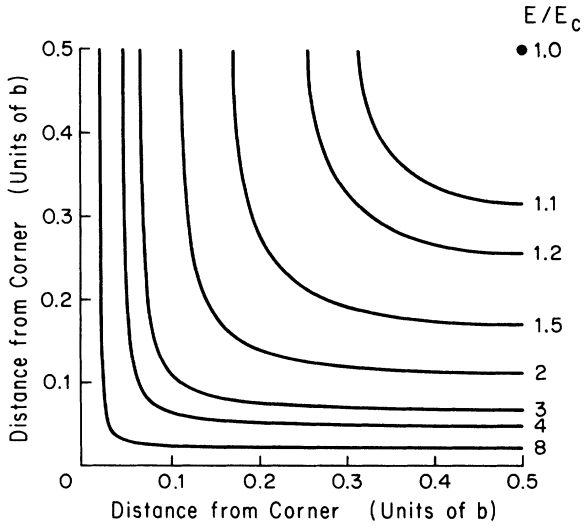

FIG. 5. One-fourth of a mesh opening, showing the electric field scaling. The field magnitude at the center of the opening is $E_c=8\sqrt{2}N\mu/b$.

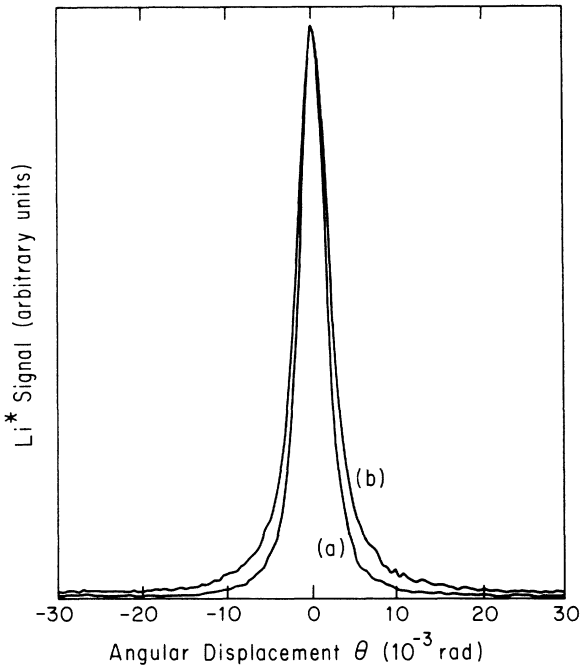

FIG. 6. Spreading of the Li* beam. Angular distribution in the horizontal plane, showing that the spreading of the beam due to the mesh is a small effect: (a) mesh removed (inner trace); (b) mesh in place (outer trace). These measurements, normalized for equal magnitudes at $\theta=0$, were made with narrower collimating slits than those described in Sec. V.

an excited atom with $n\approx 35$ will be field-ionized under the same conditions, so that the loss of signal can easily be observed in the mesh experiments to be described in Sec. VI.

High-Rydberg atoms, known to be deflected in atomic collisions,[12] will also be deflected as they pass through the mesh. The transverse forces are due to image charges, via the Van der Waals potential, and to inhomogeneous electric fields due to adsorbates on the mesh. The latter effect dominates under the conditions of our experiments. As in the case of charged particles, the high-Rydberg atoms tend to be deflected through small angles. The observed spreading of the beam due to the mesh is a small effect, as shown in Fig. 6, which documents the profile of the atomic beam. Momentum transfer thus cannot account for the reduction of the Li* signal in the experiments to be described. A detailed analysis of the angular distributions is in preparation.[13]

IV. RELATION OF SURFACE DIPOLE DENSITY TO MESH TRANSMISSION

The Au mesh used in our experiments is available from Buckbee Mears Co. as type MG-47, which has square openings and is electroformed on a Ni substrate. Scanning electron micrographs were made in order to check the dimensions of the mesh. The measurements obtained are a period $\lambda=12.9\pm0.1$ μm, strand width $b=6.45\pm0.20$ μm, and thickness $d=2.1\pm0.3$ μm. Since $\lambda\cong 2b$, the width of an opening may also be taken to be b. The area of a mesh opening is b^2, with a unit-cell area $(2b)^2$, so that $\frac{1}{4}$ of the total area is open and the geometrical transmission is $T_0=0.25$.

The effective transmission of the mesh for a given atomic state is proportional to the area enclosed by the electric field contour (as in Figs. 4 and 5) at the ionization threshold for this state. The area function can be found numerically by first generating a set of electric field contours and then integrating to find the area within each contour. Within an opening in the mesh, the fields are comparable to those within a single square hole in an infinite dipole plane, as calculated in Appendix B. Figure 7, obtained from these results, shows the effective area A enclosed by a contour at electric field E. The effective area is zero for states which are ionized below the field E_c at the center of the opening.

Surface-ionization effects tend to be small, limiting A to a maximum value $A_{\max}=(b-2\delta)^2$, where the characteristic wave-function radius δ is given as $\delta\cong 4.5n^2a_0$ in Ref. 10. The corresponding maximum transmission is $T_{\max}\cong 0.25-\delta/b$, where $\delta/b\cong 0.05$ under our experimental conditions (with $n\approx 35$), so that $T_{\max}\cong 0.2$.

A relation between the surface density of atomic dipoles and the transmission of the mesh can be obtained from measurements of the effect of known electric fields on the incident atomic beam. Figure 8 shows the variation of the beam flux (under the experimental conditions described in Sec. V) when the Li* beam passes through a transverse electric field. The ordinate $P(E)$ is the probability of survival, or the fraction of the Li* atoms not field ionized when the beam passes through an electric field E. If the area within a mesh opening is divided into small regions of area dA, each bounded by a pair of constant-field contours, the contribution to the mesh transmission from this area is $dT=P(E)dA/4b^2$. Therefore the transmission of the entire mesh can be

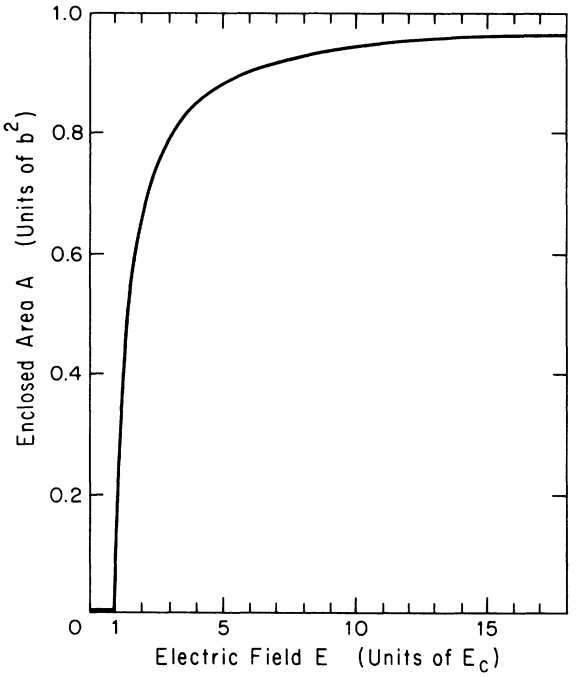

FIG. 7. Effective open area. Plot of the area enclosed by an electric field contour at field E, for a square mesh opening. The effect of surface ionization is not shown.

written

$$T=\frac{1}{4b^2}\int_{E_c}^{E_i}P(E)dA$$
$$=\tfrac{1}{4}\int_1^{\mathcal{E}_i}P(\mathcal{E}E_c)\left[\frac{d(A/b^2)}{d\mathcal{E}}\right]d\mathcal{E}\ , \qquad (12)$$

where $\mathcal{E}=E/E_c$ and $\mathcal{E}_i=E_i/E_c$, with E_i representing the value of E at the maximum mesh-to-atom distance at which surface ionization can occur.

It is a straightforward procedure to evaluate the integral in Eq. (12). The experimental data of Fig. 8 are used for $P(E)$, and the quantity in large parentheses is the slope of the function plotted in Fig. 7. The result for T in terms of E_c, plotted as T versus the absolute value of the average surface dipole-moment density, $|\langle N\mu\rangle|$, is shown in Fig. 9. Since $\delta \ll b$, the value of $\mathcal{E}_i$ is rather large and does not appreciably affect the results. In fact, $\mathcal{E}_i$ can be obtained from Eq. (8), which holds for an atom passing near the edge of a mesh opening: $E_i=2N\mu/\delta$, implying $\mathcal{E}_i=b/4\sqrt{2\delta}\cong 4$. This value of the upper limit of integration in Eq. (12), which yields $T_{\max}\cong 0.22$, is taken in Fig. 9. The initial slope of this plot shows that a significant decrease in transmission is expected during the acquisition of 10^{-2} monolayer or less, if $\mu\approx ea_0$.

This method for calibrating the experiments allows a value of $|\langle N\mu\rangle|$ to be associated with each value of T, without any need for detailed consideration of the field-ionization process, analysis of quantum-state distributions, or determination of the state dependence of the detector response. The calibration field is applied to the beam for a much longer time than the field due to the mesh (10^{-5} s versus 10^{-9} s). However, the extremely rapid increase in ionization rate with field strength results in field-ionization thresholds differing by only about 10%. The excited states tend to follow diabatic paths through the Stark manifold, and are therefore relatively insensitive to electric field slew rates. Since other uncertainties

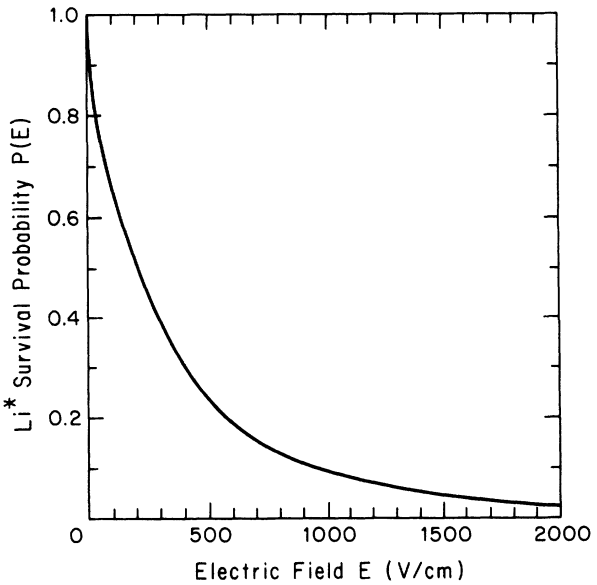

FIG. 8. Experimental results for survival probability $P(E)$ with Li* beam passing through an electric field E.

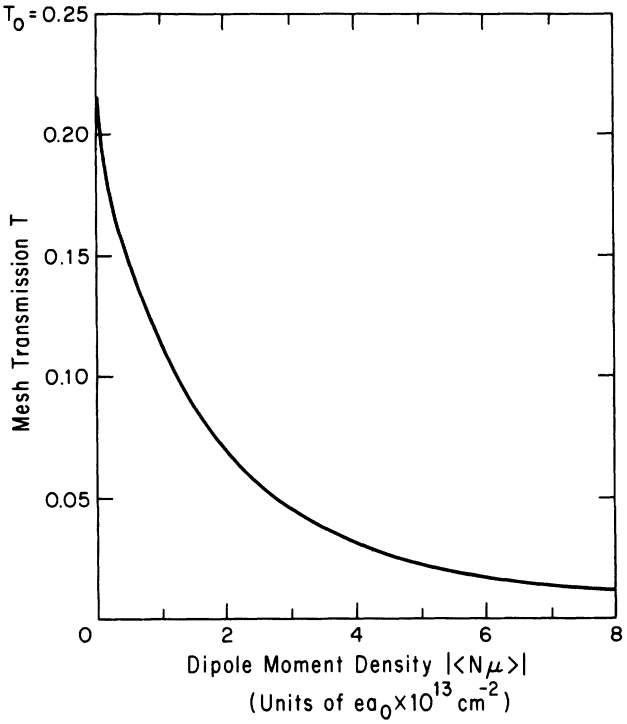

FIG. 9. Experimental calibration. Mesh transmission T as a function of $|\langle N\mu\rangle|$, the magnitude of the average surface dipole moment per unit area. Surface ionization limits T to a maximum value less than T_0.

in the calibration are of the same order, we have not made an explicit correction. In fact the slew-rate effect tends to offset another uncorrected effect, due to the finite substrate thickness [cf. the discussion following Eq. (10)].

A question for further investigation is the extent to which state changing can affect the results when very-high-n atoms pass through the localized field region near a mesh opening. In this region rapid changes occur in both the magnitude and the direction of the field experienced by the atoms, and transitions can take place near avoided crossings.[14] Field-induced transitions can generally be ignored unless they involve significant changes in ionization threshold or radiative lifetime. Blackbody radiation emitted by the walls of the vacuum chamber (at about 300 K) provides another mechanism for transitions between long-lived Rydberg states.[15] When a mesh (also at about 300 K) is inserted into the atomic-beam path, the thermal radiation field is essentially unchanged, so that the detected n-state distribution is not significantly altered.

V. EXPERIMENTAL CONDITIONS

Figure 10 shows a schematic diagram of the apparatus. Source and detector chambers are evacuated typically to 6×10^{-8} Torr. The source chamber, housing the Li atomic beam oven and high-Rydberg excitation region, is separated from the detector chamber by a bulkhead having a beam collimating slit, 3 mm wide.

Electron-impact excitation, with an electron source located 6 cm downstream from the oven, is used to produce

high-Rydberg states of Li. Earlier work under similar conditions has shown that the Li* beam consists predominantly of high-l states.[16] Electron kinetic energies are in the range from 60 to 95 eV. Ions or electrons produced in the source are removed by a transverse electric field of 15 V/cm, applied to the beam 20 cm from the oven.

The distance from the beam oven opening to the mesh is 30 cm. This dimension, together with the 3-mm bulkhead slit width, defines the angular collimation of the Li beam, which is about 20 millirad. (The distribution shown in Fig. 6 was recorded with narrower 0.3-mm slits at the oven, bulkhead, and detector.) The mesh-to-detector distance is also 30 cm.

On the mesh mount, which holds two samples, the top and bottom edges of each Au mesh are clamped between two 0.08-cm-thick Cu strips. Each sample is 1.4 cm wide and 2.5 cm high. Bolted to the clamps are lead wires to an external power supply used to heat the mesh. The top clamp is fixed to a stainless-steel frame by electrically insulated posts. At the bottom the clamp is free to slide vertically, guided by insulated posts within elongated notches. The weight of the bottom clamp keeps the mesh taut, even when its length changes as a result of thermal expansion. The stainless-steel mounting frame is attached to a rod which passes though a Wilson seal at the top of the vacuum chamber. The assembly can be moved vertically for the insertion and withdrawl of mesh samples, and may be rotated to expose either side of the mesh to the Li source.

The mesh is degassed by resistive heating, with a small voltage applied between the clamps at the top and bottom of the sample. A maximum current of 5.0 A is allowed to flow through the sample. At currents of 4 to 5 A the temperature at the center of the mesh is 700 to 900 °C, measured indirectly with thermocouples attached to the clamp at the bottom of each mesh sample and on the mounting frame. The center temperature was determined from the edge temperature by a numerical integration of the heat-flow equation, with a correction for radiation. After the degassing current has been turned off, the mesh comes to thermal equilibrium with its clamps in a characteristic time less than 1 s. The clamps, in turn, approach equilibrium with the stainless-steel mounting frame in less than 100 s. During beam transmission measurements, mesh samples are grounded and, unless otherwise noted, near the temperature of the vacuum chamber (about 30 °C).

The detector consists of a region in which the high-Rydberg states are field-ionized, along with a means of detecting the stripped electrons. Immediately preceding the detector the atomic beam passes through a second electric field, also 15 V/cm, which serves to remove ions formed in collisions along the beam path. The detector entrance slit is 3 mm in width. Once inside the detector housing, the beam enters an ionizing electric field, and the resulting electrons are counted by a Channeltron electron multiplier. The signal pulse is amplified, shaped, and sent to a 16-bit counter interfaced to a Digital Equipment Corporation PDP-11 computer programmed as a multichannel scaler. With the mesh withdrawn from the beam, signal counting rates are 2000 to 3000 s^{-1} under typical conditions. When the atomic beam is blocked, a small background signal, not exceeding 2 s^{-1}, is measured.

The electric field survival probability $P(E)$, shown in Fig. 8, was determined by monitoring the signal rate during the variation of the potential applied to the first set of plates. The distribution of principal quantum numbers in the Li* beam can also be estimated from these measurements.[17] The distribution is peaked at $n \cong 35$; the range at half-maximum extends from $n \cong 29$ to $n \cong 46$.

A Varian partial pressure gauge was used to determine the residual gas composition. The major constituents of the residual gas are H_2O and N_2, with the H_2O fraction varying from 50% in the unbaked vacuum system to less than 10% after the detector chamber has been baked for 10 h at about 80 °C. Since the role of H_2O is important, it is useful to establish the rate of incidence of H_2O on a site of atomic dimensions. The gas-particle current (number of particles per unit time) incident on an area A, from one side only, is

$$c = \frac{PA}{4kT}\left[\frac{8kT}{\pi m}\right]^{1/2}, \tag{13}$$

where P and T are the residual-gas partial pressure and absolute temperature, m is the molecular mass, and k is the Boltzmann constant. The incident time τ, defined as the average time between molecular collisions with an area of atomic dimensions, is the reciprocal of the parti-

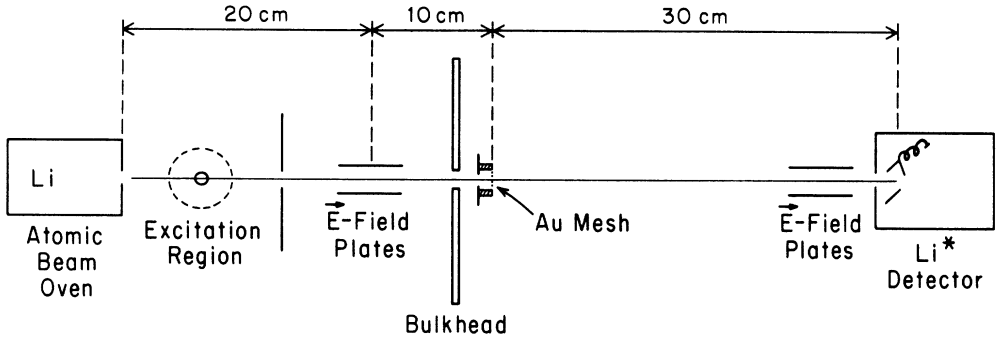

FIG. 10. Apparatus diagram showing the Li beam path (top view).

cle current, $\tau = 1/c$, where the area chosen for reference is A_s, the area occupied by a single Au atom on the (100) surface. The Au lattice constant is 4.08×10^{-8} cm, which corresponds to $A_s = 8.3 \times 10^{-16}$ cm^2. For H_2O at room temperature and a partial pressure of 3×10^{-8} Torr, the incidence time is $\tau = 80$ s. If each Au site accommodates one H_2O molecule, the monolayer accumulation time in the absence of desorption is τ/s, where s is the sticking coefficient or chemisorption probability.

The Li flux can be calculated from Eq. (13) if the right-hand side is multiplied by $A_0/\pi r^2$, where A_0 is the area of the oven opening and r is the distance from the oven. The absolute temperature T and vapor pressure P now refer to conditions within the Li oven. The right-hand side of Eq. (13) may also be modified by a channel factor;[18] however, this factor was determined experimentally to be 1.0 ± 0.1, by long-term monitoring of the oven contents at known temperatures. At the position of the Au mesh, the Li incidence time ranges from 24 to 870 s, corresponding to oven temperatures of 515 and 410 °C, respectively. When mesh transmission experiments are performed, the detector is centered with respect to the Li* beam and counts are recorded in computer memory locations (channels) corresponding to equal time intervals.

VI. EXPERIMENTAL OBSERVATIONS AND INTERPRETATION

The transmission of a newly installed mesh sample is significantly less than the geometrical value ($T_0 = 0.25$), as noted in Ref. 3. Prior to degassing, the mesh sample may have a transmission as low as $T \approx 0.01$; however, when the mesh is heated to 200 °C, the transmission rises dramatically to about 0.15. In experimenting with partially degassed mesh samples, we have found that either an increase or a decrease in transmission may occur as a result of mesh heating, depending on the history of the sample. An increase would be expected if heating desorbs a partial layer with surface dipoles aligned in the direction of the remaining layer, whereas a decrease would be observed if the dipolar field due to the desorbed layer had opposed the field due to the remaining layer.

A mesh sample is found to have reproducible properties after its surface has been degassed (and possibly annealed) by heating for 10 h at about 800 °C. When thoroughly degassed samples are studied, a standard sequence of steps is followed in each 200-channel run.

(1) A heating current of 5 A is applied to the mesh for about 5 min before it is lowered into the beam path. The purpose of this step is to degas the mesh at a temperature in excess of 700 °C along most of its length. (Under these conditions the degassing is more complete than in the preliminary experiments described in Ref. 3.)

(2) While the mesh is being degassed, counts are recorded in the first channels of the computer memory bank. These data are used in normalization, allowing the absolute transmission to be calculated. They will also be compared with results from the end of the run, for a check of Li* beam stability [cf. step (6)].

(3) The mesh sample is lowered into the beam path.

(4) The heating current is immediately switched off (for a mesh temperature of 25 to 40 °C) or reduced to the value to be used during the course of the run.

(5) Data are gathered until about channel 190. A constant dwell time, usually 20 s per channel, is maintained.

(6) The mesh is withdrawn and the direct-beam signal is counted in the remaining channels, for normalization.

Conditions which can be varied between runs include mesh position, heating current, Li flux, elapsed time between removal of heating current and beam exposure, and the pressure and species of incident atoms or molecules.

Figure 11 shows the time dependence of the transmission, observed with a degassed mesh. The right vertical scale indicates the number of counts received at 20 s per channel, whereas the left scale shows the transmission, calculated by dividing the signal rate with the mesh inserted by the rate with the mesh withdrawn. Points recorded at the beginning and end of each bank (for tests of beam stability and calibration) are plotted above a break in the scale. In all of the runs to be described, the Li* beam was stable to within 3%. For this reason the normalization channels are omitted from the remaining figures showing experimental results. When the data in Fig. 11 were taken, the average incidence time required for H_2O on a single Au surface site was $\tau_w \cong 60$ s, and the oven temperature was adjusted to provide a Li incidence time $\tau_L \cong 250$ s.

In Fig. 11 the transmission T, initially 0.20, falls to a minimum of about 0.15 in a time interval of 300 s, then rises to a sharp cusp with a value of 0.19 after 400 s, falls again (more slowly) to a minimum of 0.12 after 1200 s, and finally rises a second time, approaching a constant value of 0.18. This double-dip sequence is reproducible, having been recorded in more than 50 independent scans.

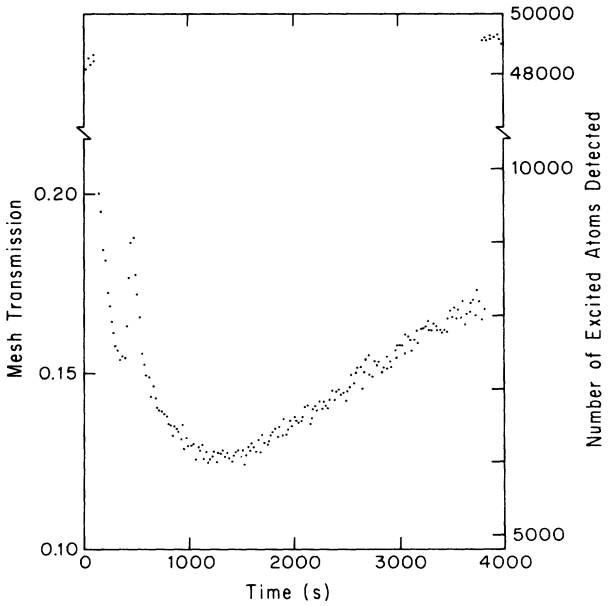

FIG. 11. Transmission measured as a function of time for a degassed mesh sample.

Figure 12 shows the results of three runs, in two of which the atomic beam was blocked and the mesh allowed to cool for a few minutes before removal of the beam stop. In each case the heating current was turned off at $t=70$ to 80 s. Trace (a) was recorded with zero time delay; in (b) and (c) the delays are 200 and 320 s, respectively. The data with delays between mesh cooling and Li beam exposure closely track the plot in which Li exposure immediately follows the cooling. As previously noted, after the heating current is turned off, mesh clamps and mounting frame come to thermal equilibrium with a characteristic time of about 100 s, corresponding to approximately five data channels. Clearly, the transmission event sequence is initiated by removal of the heating current from the mesh, and not by its exposure to the Li beam. We conclude that the background gas is primarily responsible for the time variation of T, while effects from Li may also be present.

A possible explanation for the double-dip behavior, discussed in Sec. VII, is that the transmission decreases as a partial monolayer of H_2O accumulates on the mesh surface facing the Li beam source, which bears a permanent layer of LiOH or a similar Li compound such as Li_2O, due to the reaction of Li with residual H_2O. The subsequent increase in transmission would then be due to the accumulation of a monolayer of H_2O on the detector side of the Au mesh, which does not have a permanent layer, and for which the sticking coefficient is expected to be smaller. The H_2O dipole moments on the two sides of the mesh are opposite in direction and tend to cancel, with a cusp formed as the net surface dipole moment changes sign. With the assumption of H_2O sticking coefficients $s_w \approx 0.1$, the observed characteristic times of 300 to 500 s are consistent with the monolayer accumulation time τ_w / s_w for H_2O. The final rise in T can be attributed to a decrease in the dipole moments as the coverages approach unity.

The field-ionization rate necessary for this explanation follows directly from an estimate of the time of passage δt for a Li*-beam atom through a mesh opening. The time estimate is given by $\delta t = d/v$, where $d = 2.1 \times 10^{-4}$ cm is the mesh thickness and $v \cong 2 \times 10^5$ cm/s is a typical speed for an atom in the beam. The result, $\delta t \approx 10^{-9}$ s, requires an ionization rate on the order of 10^9 s^{-1}, which is comparable to observed rates.[7]

The foregoing interpretation of the cusp can be assessed by means of the calibration between $|\langle N\mu \rangle|$ and T described in Sec. V. When the transmission values in the data of Fig. 11 are converted to dipole densities through the calibration curve shown in Fig. 9, the data can be transformed into a plot of $|\langle N\mu \rangle|$ versus time, as indicated in Fig. 13(a). Note, however, that although the value of $|\langle N\mu \rangle|$ approaches zero at the cusp, the sign of $\langle N\mu \rangle$ cannot be obtained directly from the plot. Figure 13(a) can be redrawn so that $\langle N\mu \rangle$ is initially negative, changing sign at the cusp, and then becoming positive. This choice of sign convention will be discussed in Sec. VII. The smooth continuity of this result, shown in Fig. 13(b), supports the interpretation of a sign change at the cusp in Fig. 11.

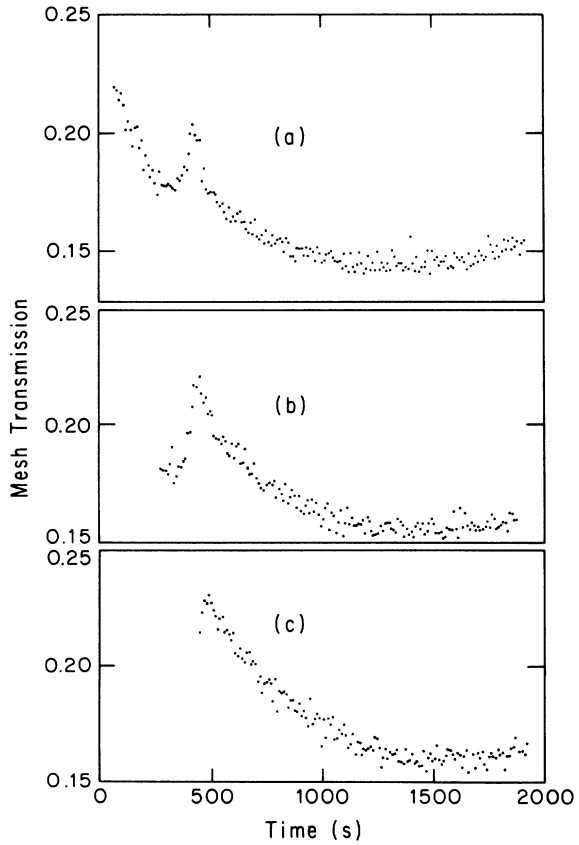

FIG. 12. Transmission vs time, showing the effect of delaying the exposure of the mesh to Li. (a) No time delay, (b) 200 s delay, and (c) 320 s delay.

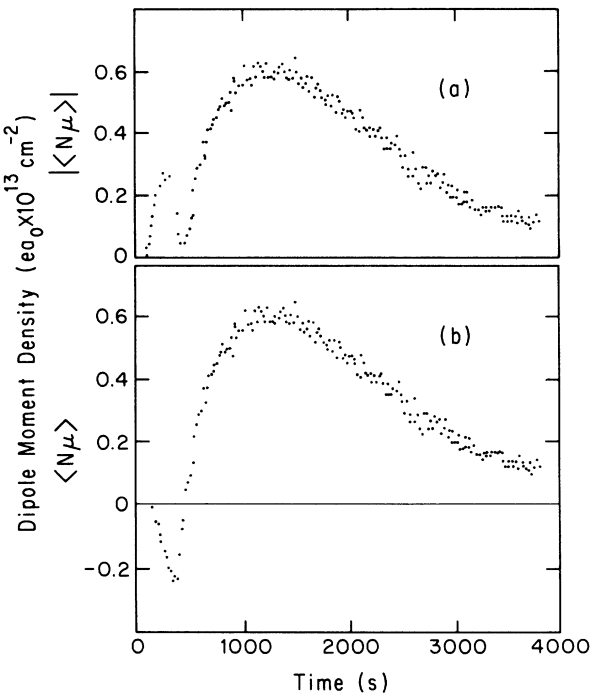

FIG. 13. Data from Fig. 11 plotted to show (a) $|\langle N\mu \rangle|$ vs t, and (b) $\langle N\mu \rangle$ vs t, with a sign change at the cusp.

Several additional comments should be made concerning the experimental results. Data sampled at discrete times do not necessarily reveal the full value of T at the cusp, where the counting rates are rapidly changing and may vary significantly during the 20-s dwell time. At the cusp, where the dipole fields are small, the value of T may also be sensitive to residual fields, as would be expected if spatial fluctuations are present in the surface dipole-moment density. It should also be noted that the mesh temperature may not stabilize until several points have been recorded at the beginning of each run. For this reason the initial values of T, immediately after the degassing current is turned off, may be higher than if the final mesh temperature (about 30 °C) had been attained. A final point is that since the mesh is introduced into the Li beam in the midst of a data channel, the starting time for the event sequence is uncertain by as much as one complete dwell interval (20 s).

It is possible to study the time dependence of the surface dipole-moment density for H_2O, by varying the partial pressure of H_2O within the vacuum chamber. As Fig. 14 indicates, changes in the H_2O incidence time affect primarily the initial behavior of the mesh transmission. An increase in partial pressure by a factor of 1.6 (a decrease in H_2O incidence time from 105 to 65 s) reduces the time interval for the initial peak from 320 to 200 s, without significantly affecting the longer-term trend.

Three runs with different oven temperatures are plotted in Fig. 15, which shows the effect of variation of the Li flux reaching the source side of the mesh. These plots show that adsorbed Li has little effect prior to the cusp, but does affect the transmission at longer times. At the highest flux indicated, the average dipole-moment density appears to change sign twice, with a second sign change occurring after about 2500 s have elapsed. The magnitude of the long-term surface dipole moment increases as the Li flux decreases.

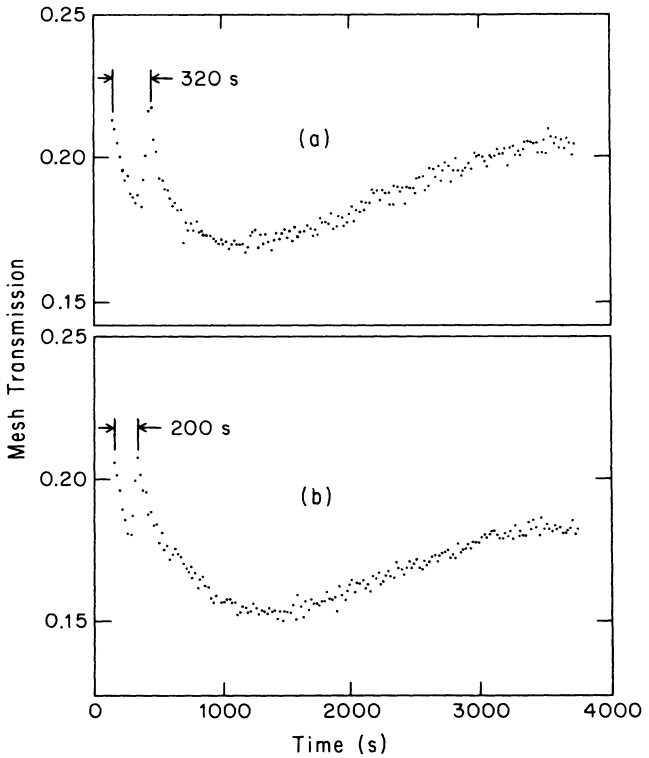

FIG. 14. Transmission with H_2O flux varied: (a) incidence time $\tau_w = 105$ s, (b) $\tau_w = 65$ s.

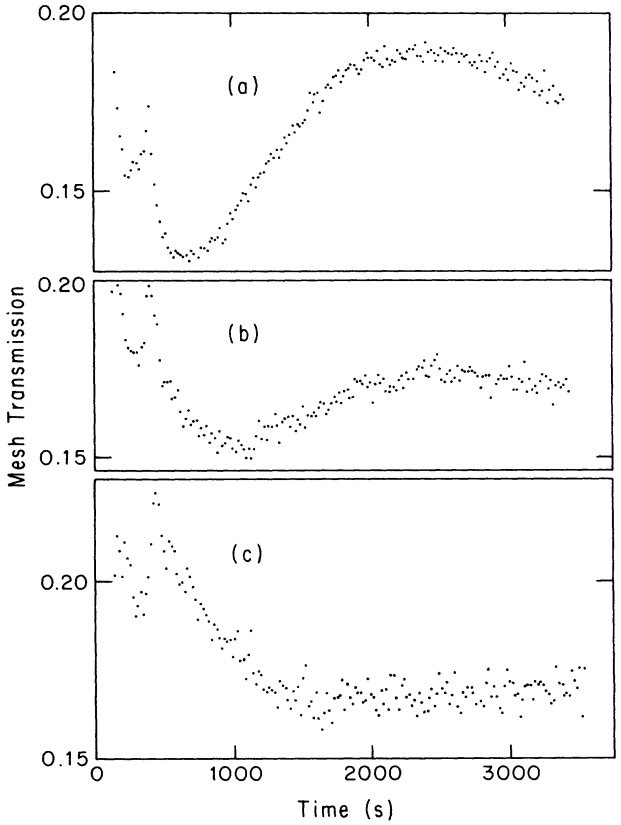

FIG. 15. Transmission with Li flux varied: (a) incidence time $\tau_L = 100$ s, (b) $\tau_L = 290$ s, and (c) $\tau_L = 540$ s.

The effect of mesh temperature is indicated in Fig. 16. At 50 °C (center of mesh), the dips are less pronounced, but the timing does not change appreciably. At 100 °C or higher, the dips disappear altogether and the transmission is near 0.22. These results are compatible with a desorption rate for H_2O which increases with mesh temperature, reducing the ultimate coverage. Surface ionization remains as a mechanism for signal loss, and the transmission can never exceed the surface-ionization-limited value. The data of Fig. 16 suggest that deeper dips in the transmission may be obtained in experiments with a cooled mesh.

Figure 17 shows the effect of reversing the orientation of the mesh, after the permanent layer has formed on one side. These results were recorded immediately after the reversal of the mesh, so that the clean Au surface faces the source and the permanent layer faces the detector. It is interesting that the cusp is no longer present. One might expect the sticking coefficient to increase for H_2O on the detector side as a permanent layer forms, during the interval required for several runs. In fact this behavior was observed in subsequent runs, with the initial fall, dip, and recovery taking place progressively more rapidly.

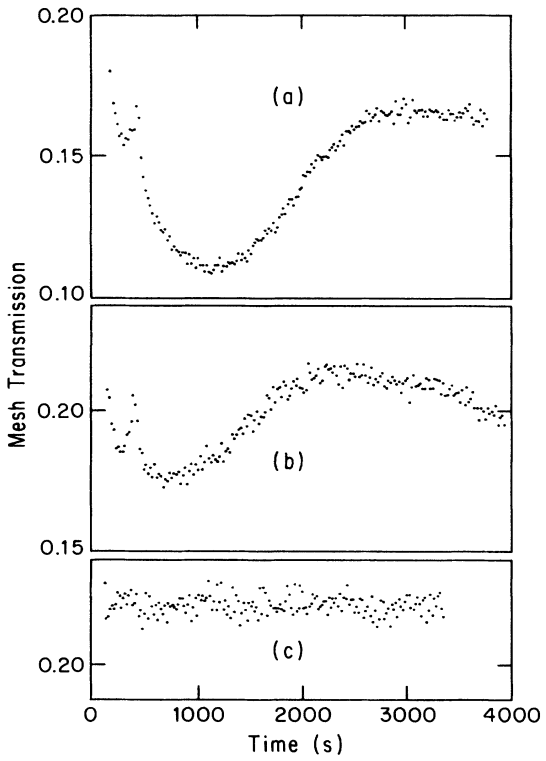

FIG. 16. Transmission with mesh temperature varied: (a) 35 °C, (b) 50 °C, and (c) 100 °C at the center of the mesh.

VII. MODEL CALCULATIONS AND ANALYSIS

The transmission of the mesh can be calculated in a simple Langmuir-type model which accounts for the effects of H_2O and Li adsorption on the mesh surface. A distinctive feature is that the H_2O adsorption rates are unequal on the two sides of the mesh. By means of this model it is possible to calculate the reduction in transmission due to field ionization of the excited Li* atoms.

When an atom in the Li beam reaches the mesh surface at a location already occupied by a H_2O molecule, the two can combine to form an adsorbate such as LiOH or an oxide of Li (e.g., Li_2O), which would have low vapor pressure and thus be relatively permanent. Such a layer would not be removed during the subsequent heating of the mesh, which desorbs H_2O from both sides at the beginning of each run. The time required for the formation of this nondegassable layer can be estimated from solutions of rate equations for the coverages. It is evident that the layer would form in a time which is comparable to the H_2O monolayer accumulation time $\tau_w = 1/s_w c_w$ or the Li incidence time $\tau_L = 1/c_L$, whichever is longer. Since both quantities are typically 10^3 s, the permanent layer is believed to form in this relatively short time, and to remain on the source side of the mesh during all subsequent measurements on this sample.

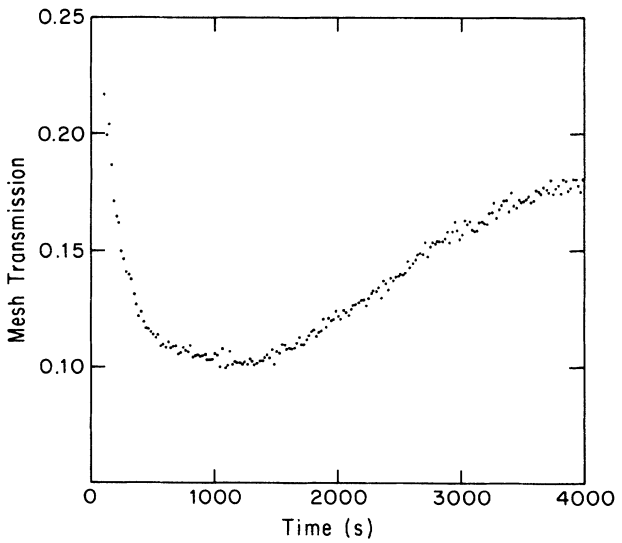

FIG. 17. Transmission with mesh orientation reversed.

In the model, adsorption on the detector side of the mesh is described by a coverage Θ_{wd} for H_2O on clean Au. On the source side the coverages are denoted by Θ_p for the permanent layer, Θ_L for Li, and Θ_{ws} for H_2O. The relevant particle currents are c_L for Li and c_w for H_2O. Two sticking coefficients are needed: s_{wd} for H_2O incident on Au on the detector side of the mesh and s_{wp} for H_2O on the permanent layer on the source side. It is assumed that when Li is incident on any surface site, or when H_2O is incident on a Li site, chemisorption will take place with a sticking coefficient equal to unity. For simplicity, desorption terms are omitted.

On the detector side of the mesh, where no Li is incident and only Θ_{wd} needs to be considered, the time dependence is given by

$$\dot{\Theta}_{wd} = s_{wd} c_w (1 - \Theta_{wd}) \ . \tag{14}$$

With the initial condition $\Theta_{wd} = 0$, the solution is

$$\Theta_{wd} = 1 - e^{-s_{wd} c_w t} \ . \tag{15}$$

For the source side of the mesh, the model is set up to account for adsorbates which can form after the complete permanent-layer substrate has formed. The differential equations are

$$\dot{\Theta}_L = c_L \Theta_p - c_w \Theta_L \ , \tag{16}$$

$$\dot{\Theta}_{ws} = s_{wp} c_w \Theta_p - c_L \Theta_{ws} \ , \tag{17}$$

and

$$\dot{\Theta}_p = -c_L \Theta_p - s_{wp} c_w \Theta_p + c_L \Theta_{ws} + c_w \Theta_L \ . \tag{18}$$

Since a fixed number of surface sites is assumed, the coverages sum to unity. The solution is straightforward; initial conditions $\Theta_p = 1$ and $\Theta_L = \Theta_{ws} = 0$ are taken.

From the model we can obtain qualitative and semiquantitative insight into the time dependence of the transmission. The average surface dipole-moment density is given in terms of the coverages by

$$\langle N\mu \rangle = (\mu_w \Theta_{wd} - \mu_L \Theta_L - \mu_p \Theta_p - \mu_w \Theta_{ws}) / A_s \ , \tag{19}$$

where μ_L, μ_p, and μ_w are the magnitudes of the atomic or molecular dipole moments of Li, Li_2O (or LiOH), and H_2O, respectively, and where A_s is the area of a surface

site. It is assumed that the dipole moments of both Li and H_2O are similarly oriented on the surface, with the positive charge outward. A sign convention is followed in which $\langle N\mu \rangle$ receives a positive contribution from such a dipole when it is present on the detector side of the mesh. The dipole moments are functions of coverage.

Computer-generated plots of $\langle N\mu \rangle$ versus t were made from Eq. (19), using the solution of Eqs. (16)–(18) for the coverages. Before the presentation of results, it is appropriate to indicate how the values for the experimental parameters were selected.

To obtain a value for μ_p, we note that in Fig. 11 the transmission of about 0.20 at $t=0$ is very close to the surface-ionization-limited value discussed in Sec. IV. Since $\Theta_p=1$ is assumed at $t=0$, we conclude that $\mu_p < 10^{-4} e a_0$ and therefore set $\mu_p=0$ in the model.

In general, surface dipole moments decrease monotonically as the coverage increases.[19,20] In the model we have used a Lorentzian form

$$\mu=\frac{\mu_0}{1+\beta\Theta^2} \tag{20}$$

to describe the dipole moments of both H_2O and Li. A similar Θ dependence follows from adsorbate polarizability calculations based on a Topping field determination of each adsorption site.[19] For the source side of the mesh, Θ in the denominator of Eq. (20) is taken to be the sum of the coverages for H_2O and Li. Theoretical cluster calculations[21] for H_2O on Al have yielded values for μ_0 in the range from $0.02 e a_0$ to $0.16 e a_0$. For H_2O the model values are $\mu_0=0.08 e a_0$ on the source side of the mesh and $\mu_0=0.10 e a_0$ on the detector side, with $\beta=4$ in both cases. Gerlach and Rhodin[22] have measured the coverage dependence of the surface dipole moments for alkali atoms on a Ni substrate. Extrapolations for Li suggest that the values of μ will drop by a factor of about 2 between $\Theta=0$ and $\Theta=1$, and therefore we have taken $\beta=1$ for Li, together with a value $\mu_0=0.04 e a_0$ for the permanent-layer substrate, which gives a good fit to the experimentally observed transmission values.

The sticking coefficients can be chosen to reproduce the observed timing of the events. If the trial values $s_{wp}=0.2$ and $s_{wd}=0.1$ are used, the model predicts variations of $\langle N\mu \rangle$ with time as shown in Fig. 18, where transmission values are obtained through the calibration of Fig. 9. These results from the model (plotted with the adsorption beginning at $t=0$ rather than at $t \cong 100$ s as in the measurements) are compatible with the experimental results of Fig. 14. Figure 18 shows results from the model for two values of the H_2O particle current c_w. As in the data of Fig. 14, the changes occur primarily at early times, with the cusp appearing later if the particle current is decreased. The similarity of Figs. 14 and 18 suggests that reasonable values of the model parameters have been chosen.

Plots from the model for three values of the Li particle current c_L are shown in Fig. 19. The results are consistent with the data of Fig. 15. In the model, as in the experiments, large changes in the Li particle current have only a small effect on the time at which the cusp is observed, but the behavior at later times is significantly affected. In both figures the upper trace (a) shows a possible second change in the sign of $\langle N\mu \rangle$, occurring at $t \cong 2000$ s.

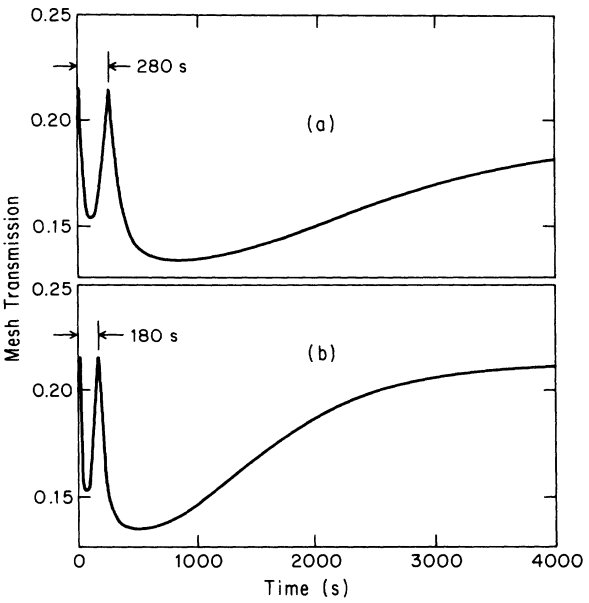

FIG. 18. Model calculations of mesh transmission, showing variation with H_2O particle current. (a) $\tau_w=120$ s, (b) $\tau_w=75$ s. Compare with Fig. 14.

Figure 20 shows predictions from the model immediately after the mesh orientation has been reversed, so that

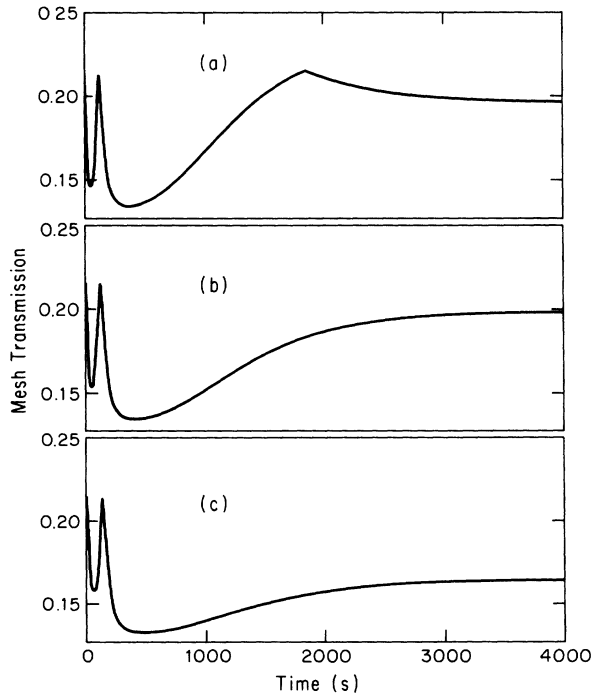

FIG. 19. Predictions from the model for three values of the Li particle current. (a) $\tau_L=100$ s, (b) $\tau_L=200$ s, and (c) $\tau_L=400$ s. Compare with Fig. 15.

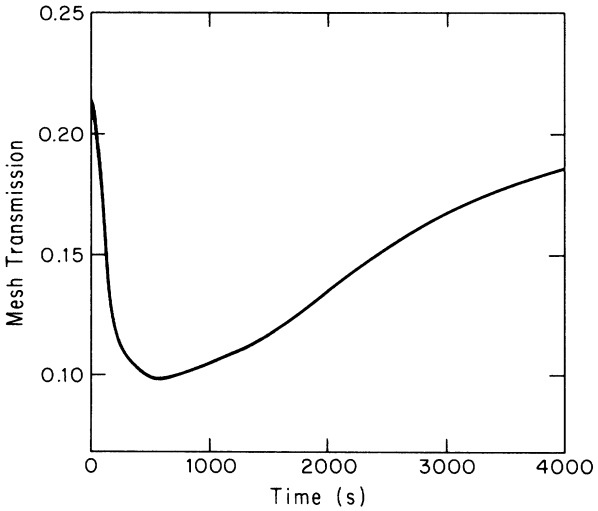

FIG. 20. Predictions from the model for reversed mesh orientation. Compare with Fig. 17.

the permanent layer now faces the detector. The cusp is no longer present, and the calculations are in good agreement with the experimental data of Fig. 17.

When Li incident on H_2O is not chemisorbed, it may diffuse into the Au mesh. The diffusion constant for Li in Au is $D \gtrsim 4\times10^{-15}$ cm^2/s at room temperature.[23] Thus surface Li adatoms might diffuse into the substrate, with subsequent loss of their contribution to the surface dipole field, but it is also possible that Li cannot readily diffuse through the permanent layer. If the effects of Li diffusion were to be included in the model, a term $\gamma_L\Theta_L$ would be subtracted from the right-hand side of Eq. (16) and added to the right-hand side of Eq. (18). The inclusion of these terms is similar to a shift in the value of c_L, and therefore it is difficult to determine whether Li diffusion plays a significant role. As seen in Figs. 18–20, the experimental results are well described by a model in which the effects of diffusion and desorption are not included.

The following scenario is compatible with the time development of $\langle N\mu\rangle$. When the heating current is removed, the mesh temperature decreases and H_2O begins to accumulate on both sides of the mesh. If $s_{wp} > s_{wd}$, the initial H_2O layer builds up more rapidly on the source side than on the detector side, and the net surface-dipole-moment density $\langle N\mu\rangle$ becomes negative, causing a decrease in the mesh transmission. After a longer time has elapsed, H_2O adsorbed on the detector side of the mesh becomes important, contributing dipole moments which are oppositely directly with respect to those on the source side. Because of this cancellation, $\langle N\mu\rangle$ attains a minimum and then becomes less negative. As $|\langle N\mu\rangle|$ decreases, the transmission consequently increases. The field contribution of the detector-side layer can increase to the point where it virtually cancels the source-side field. The direction of the net dipole moment can then change sign. When $\langle N\mu\rangle$ passes through zero, the transmission increases to a maximum and then suddenly begins to drop, forming the cusp observed in Figs. 11–16. The presence of Li assists in the reduction of $\langle N\mu\rangle$ during the latter portion of the run. As the coverages increase further, the surface dipole moments μ tend to diminish in magnitude. Therefore, after a significant portion of a monolayer covers both sides of the substrate, $|\langle N\mu\rangle|$ is expected to decrease again, accounting for the final increase in the transmission.

At this stage in our understanding of these processes, detailed questions of surface chemistry are of less concern than the fundamental point that high-Rydberg atoms can serve as probes of adlayers on the surface of a fine mesh.

VIII. SENSITIVITY ESTIMATES

The experiments provide strong evidence that the Li* beam can detect surface dipole fields which extend over a small region such as a mesh opening, with dimensions of 10^{-3} to 10^{-4} cm. Our calculations support the identification of field ionization as an explanation for the observed variations in mesh transmission. An adlayer of H_2O, together with a small contribution due to Li from the atomic beam, generate an electric field which can account for the loss of Li* atoms.

Estimates of the experimental sensitivity will illustrate the value and limitations of this technique. Two measures of the sensitivity will be considered: (1) the absolute sensitivity, or minimum detectable surface dipole moment density; and (2) the differential sensitivity, or minimum detectable change in dipole moment density. It will be assumed that the mesh has square geometry with the dimensions given.

The absolute sensitivity is limited by surface ionization near the edges of each mesh opening. At a small distance x from the edge, the electric field is found from Eq. (8) to be $E \cong 2|\langle N\mu\rangle|/x$, whereas from Sec. IV the maximum surface ionization distance is $\delta \cong 4.5n^2a_0$. The requirement $x > \delta$ implies a minimum detectable surface dipole density $|\langle N\mu\rangle|_{\min} \cong E_n\delta/2$, where E_n is the minimum electric field at which the excited atoms are ionized. If $E_n \cong (6\times10^8$ V/cm$)/n^4 \cong 0.12e/n^4a_0^2$, then the absolute sensitivity estimate is

$$|\langle N\mu\rangle|_{\min} \cong \frac{0.27e}{n^2a_0} \cong \frac{8ea_0}{n^2A_s}\ , \tag{21}$$

where the area of a surface site on Au is $A_s = 8.3\times10^{-16}$ cm$^2 \cong 30a_0^2$. At $n = 35$ and 100, the results are $|\langle N\mu\rangle|_{\min} \cong 7\times10^{-3}ea_0/A_s$ and $8\times10^{-4}ea_0/A_s$, respectively.

In the determination of differential sensitivity, excited-atom counting rates determine how small a change in transmission is statistically significant. The highest differential sensitivity will be achieved in experiments with state-selected atomic beams, in which all of the Rydberg states might have similar thresholds E_n for field ionization. In this case $P(E)$ can be taken to be unity if $E < E_n$ and zero if $E > E_n$. Then Eq. (12) reduces to $T = A/4b^2$, with the effective area A evaluated for the electric field contour at E; and a function derived directly from Fig. 7 replaces Fig. 9. The resulting plot of T versus $|\langle N\mu\rangle|$ is shown in Fig. 21, where the flat region at the

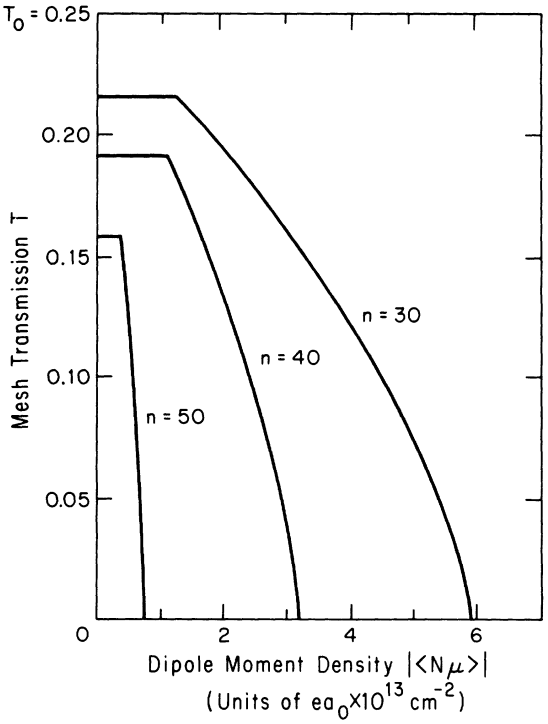

FIG. 21. T vs $|\langle N\mu \rangle|$ for several state-selected high-Rydberg beams.

upper left shows the effect of surface ionization.

The mesh transmission is most sensitive to changes in $|\langle N\mu \rangle|$ near the cutoff point in Fig. 21. In this region only atoms incident on the central portion of a mesh opening can be transmitted without being ionized. The field contours near the center are approximately circular, and the area enclosed by a contour can be obtained from a Taylor-series expansion of Eq. (A6). The resulting spatial dependence of the electric field magnitude near the center of a mesh opening is $E(r)=E_c(1+4r^2/b^2)$, where r is the distance from the center, in the $z=0$ plane. This relation defines the effective open area $A=\pi r^2$, where $A \ll b^2$. The transmission is then

$$T=\frac{A}{4b^2} \cong \frac{\pi}{16}\left[\frac{E_n}{E_c}-1\right]=\frac{\pi}{16}\left[\frac{bE_n}{8\sqrt{2}\,|\langle N\mu \rangle|}-1\right] \tag{22}$$

in the region of maximum slope magnitude. The differential sensitivity is therefore

$$\Delta|\langle N\mu \rangle|_{\min} \cong \left|\frac{d|\langle N\mu \rangle|}{dT}\right| \Delta T \cong \frac{\sqrt{2}E_n b}{\pi}\Delta T \ . \tag{23}$$

If $\Delta T = 10^{-2}$ can be resolved, then

$$\Delta|\langle N\mu \rangle|_{\min} \cong (2\times 10^3)\frac{ea_0}{n^4 A_s} \ . \tag{24}$$

For $n=35$ and 100, respectively, the predictions are $\Delta|\langle N\mu \rangle|_{\min} \cong (1.3\times 10^{-3})ea_0/A_s$ and $2\times 10^{-5}ea_0/A_s$. These estimates of the differential sensitivity indicate the change in surface dipole-moment density which will result in a transmission difference $\Delta T=0.01$. At counting rates above 10^4 per channel, a change of 10^2 per channel is both observable and statistically significant.

The calculations show that it is advantageous to make the principal quantum number n as large as possible, although the mesh spacing b must be sufficiently large to insure that a major portion of the beam is not lost to surface ionization. Equations (21) and (24) also indicate that under suitable conditions the experiments will be more sensitive to changes in surface dipole density than to absolute values. The absolute sensitivity estimate, Eq. (21), indicates that in an experiment in which an adequate signal rate can be obtained with $n=100$, adsorbed atoms or molecules with dipole moments as small as $8\times 10^{-4}ea_0$ can be detected at monolayer coverage on a substrate of Au, or adsorbates with dipole moments as large as ea_0 can be detected at 8×10^{-4} monolayer. Detection thresholds can be significantly lower in the differential mode, as shown by Eq. (24). For example, $\Delta|\langle N\mu \rangle|_{\min} \cong \frac{1}{40}|\langle N\mu \rangle|_{\min}$ at $n=100$. Under favorable conditions, changes in a surface layer might be detectable at the level of 10^{-4} to 10^{-5} monolayer. Since a typical atomic spacing at 10^{-5} monolayer is about 10^{-5} cm, which is small in comparison with the mesh dimension b, the treatment of the adsorbate as a continuous dipole layer is still valid.

An alternative experimental arrangement may be possible with a state-selected high-Rydberg beam and a detector field set just below the threshold for detection (in the absence of the mesh). When the mesh is inserted into the beam path, the electric field pulse experienced by the atoms may induce transitions into detectable states. This method would lead to a detected signal on top of a zero background, rather than a change in an already significant counting rate.

Although the demonstration experiments are far from the calculated limit of sensitivity, they confirm that variations in the transmission of a mesh can be observed on a time scale much shorter than the monolayer adsorption time. This technique appears to be especially well suited to measurements of the orientations of adsorbate dipole moments. With a gas source capable of alternately depositing layers of different atoms or molecules on the detector side of the mesh surface, combinations of several adsorbate species should give a clear indication of the relative signs of the dipole moments on Au (or other substrate). When the second species is added to a partial monolayer of the first, the transmission will decrease or increase according to whether the dipoles are parallel or opposite in orientation. If the orientation is known for a reference adsorbate (any one species), then orientations can be inferred for the others. Absolute values of μ can also be extracted if the coverage can be determined.

Further investigations utilizing this method may be capable of revealing dynamic changes in surface structure resulting from processes such as adatom rearrangement, desorption, diffusion, and chemical reactions on surfaces.

APPENDIX A: FIELD CALCULATION FOR A SURFACE DIPOLE LAYER ON A CYLINDER

The electrostatic potential due to an infinitely long grounded cylinder of radius a, covered by a nonuniform dipole layer of surface charge density $\sigma=\sigma_0\cos\psi$ surrounding one side ($-\pi/2<\psi<\pi/2$), may be calculated from the two-dimensional potential due to a line of charge outside a conducting infinitely long cylinder. The coordinates and geometry are shown in Fig. 22. This electrostatic potential, found by the method of images, is

$$V_{\delta\lambda}=\delta\lambda\ln\left[\frac{a^2r^2+a^2R^2-2a^2rR\cos\theta}{r^2R^2+a^4-2a^2rR\cos\theta}\right], \tag{A1}$$

where R is the distance from the cylinder axis to the line charge $\delta\lambda$, r is the distance from $\delta\lambda$ to the observation point, and a is the radius of the cylinder. We may take $\delta\lambda=\sigma R\,\delta\psi=\sigma_0 R\cos\psi\,\delta\psi$.

The potential due to a distribution of line charges outside a conducting cylinder is then found by integration of Eq. (A1) over ψ:

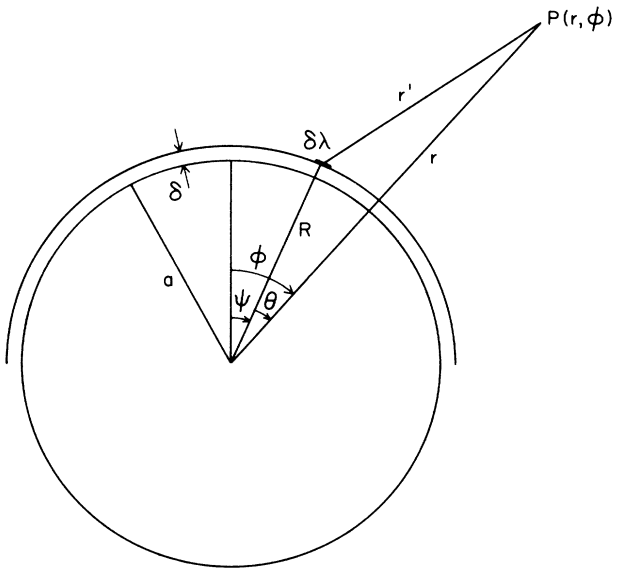

FIG. 22. Coordinates for determination of the potential at point P outside a long conducting cylinder of radius a, bearing a surface layer.

$$V(r,\phi,z)=\sigma_0 R\int_{-\pi/2}^{\pi/2}\ln\left[\frac{a^2r^2+a^2R^2-2a^2rR\cos(\phi-\psi)}{r^2R^2+a^4-2a^2rR\cos(\phi-\psi)}\right]\cos\psi\,d\psi\,, \tag{A2}$$

where $\phi=\theta+\psi$ is the azimuthal angle of the observation point. This expression is seen to satisfy the grounded-cylinder boundary condition $V(a,\phi,z)=0$ for all ϕ and z.

If we define $\delta=R-a$ to be the distance between the line charge and the surface, then the interesting case occurs when $\delta\ll a$ and $\delta\ll r-a$. Then $R\approx a$ and the effective surface density is $N=N_0\cos\psi$ for an infinitely thin dipole layer on the upper half of the cylinder. The potential is

$$V(r,\phi,z)=-\sigma_0 a\int_{-\pi/2}^{\pi/2}\ln\left[\frac{r^2+a^2+2a\delta-2ar\cos(\phi-\psi)}{r^2+a^2+2r^2\delta/a-2ar\cos(\phi-\psi)}\right]\cos\psi\,d\psi\,. \tag{A3}$$

Expansion of the integrand in the limit of small δ gives

$$V(r,\phi,z)=-2\sigma_0 a\left[a\delta-\frac{r^2\delta}{a}\right]\int_{-\pi/2}^{\pi/2}\frac{\cos\psi\,d\psi}{r^2+a^2-2ar\cos(\phi-\psi)}\,. \tag{A4}$$

If the integration is performed over θ, then $\cos\psi=\cos\phi\cos\theta+\sin\phi\sin\theta$ and $d\psi=-d\theta$, so that

$$V(r,\phi,z)=2\sigma_0\delta(r^2-a^2)\left[\int_{\phi-\pi/2}^{\phi+\pi/2}\frac{\cos\phi\cos\theta\,d\theta}{r^2+a^2-2ar\cos\theta}+\int_{\phi-\pi/2}^{\phi+\pi/2}\frac{\sin\phi\sin\theta\,d\theta}{r^2+a^2-2ar\cos\theta}\right]. \tag{A5}$$

After evaluation of the integrals, we obtain

$$V(r,\phi,z)=2\sigma_0\delta(r^2-a^2)\left[\frac{\sin\phi}{2ar}\ln(r^2+a^2-2ar\cos\theta)-\frac{\cos\phi}{2ar}+\frac{(r^2+a^2)\cos\phi}{ar(r^2-a^2)}\tan^{-1}\left[\frac{r+a}{r-a}\tan\frac{\theta}{2}\right]\right]\Bigg|_{\phi-\pi/2}^{\phi+\pi/2}. \tag{A6}$$

The following relation allows simplification of the final term:

$$\tan^{-1}x-\tan^{-1}y=\tan^{-1}\left[\frac{x-y}{1+xy}\right]+\pi H\left[\frac{\pi}{2}-|\phi|\right], \tag{A7}$$

where the principal value of the arctangent is taken. The Heaviside unit-step function $H(\pi/2-|\phi|)$ maintains the continuity of the potential. In the limit $\delta\ll a$, the dipole-moment density is given by $N_0\mu\cos\psi=2\sigma_0\delta\cos\psi$, so that $\sigma_0\delta=N_0\mu/2$.

The final result is

$$V(r,\phi,z)=\frac{N_0\mu}{2ar}\left\{(r^2-a^2)\left[\sin\phi\ln\left[\frac{r^2+a^2+2ar\sin\phi}{r^2+a^2-2ar\sin\phi}\right]-\pi\cos\phi\right]\right.$$
$$\left.-2(r^2+a^2)\cos\phi\left[\tan^{-1}\left[\frac{r^2-a^2}{2ar\cos\phi}\right]-\pi H\left[\frac{\pi}{2}-|\phi|\right]\right]\right\}. \quad \text{(A8)}$$

This expression is the basis for the potential and field plots shown in Fig. 3.

APPENDIX B: FIELD CALCULATIONS FOR PLANE DIPOLE LAYERS

The electrostatic potential due to a uniform dipole layer on a rectangular patch can be calculated directly by integration over the charge distribution. The coordinates used are shown in Fig. 23. The charge density for a dipole layer in the xy plane is

$$\rho(x,y,z)=-N\mu\frac{d}{dz}\delta(z)\ . \quad \text{(B1)}$$

If the borders of the patch are x_1, x_2, y_1, and y_2, the potential is

$$V(x,y,z)=\int_{x_1}^{x_2}dx'\int_{y_1}^{y_2}dy'\int_{-\infty}^{+\infty}dz'\frac{-N\mu(d/dz')\delta(z')}{[(x-x')^2+(y-y')^2+(z-z')^2]^{1/2}}$$
$$=N\mu z\int_{x_1}^{x_2}dx'\int_{y_1}^{y_2}dy'\frac{1}{[(x-x')^2+(y-y')^2+z^2]^{3/2}}\ . \quad \text{(B2)}$$

Care must be taken to handle correctly the various cases which arise when x and y take on values either within or outside the borders of the patch. The result is

$$V=N\mu\left[\tan^{-1}\left[\frac{(x-x_1)(y-y_1)}{z[(x-x_1)^2+(y-y_1)^2+z^2]^{1/2}}\right]\right.$$
$$-\tan^{-1}\left[\frac{(x-x_1)(y-y_2)}{z[(x-x_1)^2+(y-y_2)^2+z^2]^{1/2}}\right]$$
$$-\tan^{-1}\left[\frac{(x-x_2)(y-y_1)}{z[(x-x_2)^2+(y-y_1)^2+z^2]^{1/2}}\right]$$
$$\left.+\tan^{-1}\left[\frac{(x-x_2)(y-y_2)}{z[(x-x_2)^2+(y-y_2)^2+z^2]^{1/2}}\right]\right], \quad \text{(B3)}$$

where the principal value of the inverse tangent is to be used throughout.

The potential in Eq. (B3) can be shown by differentiation to satisfy the Laplace equation everywhere except on the patch. In addition, it has the correct discontinuity within the patch, in the plane of the dipole layer. If x and y are outside the patch boundaries, then the potential is zero at $z=0$; but if x and y are within the patch boundaries, then the potential approaches $2\pi N\mu$ from positive z and $-2\pi N\mu$ from negative z, giving the expected discontinuity of $4\pi N\mu$. A special case of the dipole patch is the limit of an infinitely long strip. If $x_1=-b$, $x_2=0$, $y_1\to-\infty$, and $y_2\to\infty$, then the result given in Eq. (3) is obtained.

If Eq. (B3) is used for the potential of a rectangular patch bearing a dipole layer, the potential within a square hole may be built up. In the case of an infinite plane the result is $V=2\pi N\mu\ \mathrm{sgn}(z)$. For a patch of finite size, the presence of a hole requires subtracting the contribution of the missing part of the plane. If the opening is bounded by $0<x<b$ and $0<y<b$, then

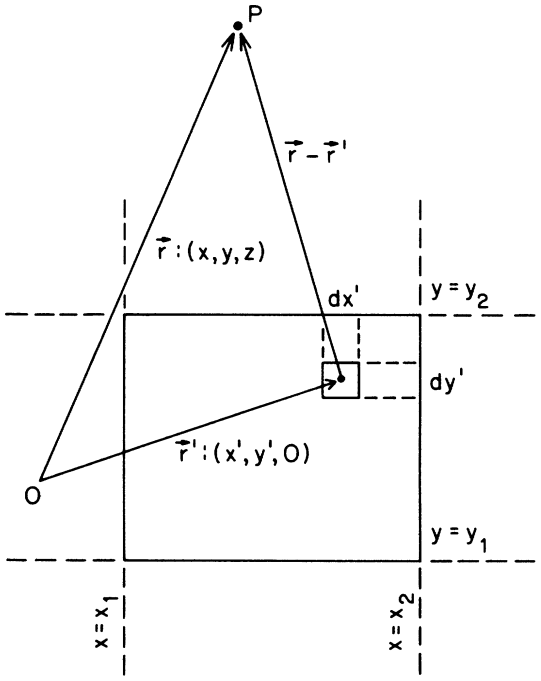

FIG. 23. Geometry for calculation of the potential at point P due to a plane dipole layer on a rectangular patch $x_1\le x\le x_2$ and $y_1\le y\le y_2$.

$$V=2\pi N\mu\,\mathrm{sgn}(z)-N\mu\left[\tan^{-1}\left[\frac{xy}{z[x^2+y^2+z^2]^{1/2}}\right]-\tan^{-1}\left[\frac{x(y-b)}{z[x^2+(y-b)^2+z^2]^{1/2}}\right]\right.$$
$$\left.-\tan^{-1}\left[\frac{(x-b)y}{z[(x-b)^2+y^2+z^2]^{1/2}}\right]+\tan^{-1}\left[\frac{(x-b)(y-b)}{z[(x-b)^2+(y-b)^2+z^2]^{1/2}}\right]\right]. \quad \text{(B4)}$$

This expression can be differentiated to find the electric field. Within the open area in the $z=0$ plane, the field is

$$E_z=-N\mu\left[\frac{(x^2+y^2)^{1/2}}{xy}-\frac{[x^2+(y-b)^2]^{1/2}}{x(y-b)}-\frac{[(x-b)^2+y^2]^{1/2}}{(x-b)y}+\frac{[(x-b)^2+(y-b)^2]^{1/2}}{(x-b)(y-b)}\right]. \quad \text{(B5)}$$

In Figs. 4 and 5 this function is plotted to show contours of constant E_z. At the center of the opening ($x=y=b/2$), the field magnitude is given by

$$E_c=8\sqrt{2}N\mu/b\ . \quad \text{(B6)}$$

APPENDIX C: DEFLECTION OF A CHARGED PARTICLE BY A DIPOLE STRIP

The technique developed for studying atom-surface interactions depends upon the rapid ionization of a high-Rydberg atom in an electric field. It is interesting to compare the sensitivity of the excited-atom technique with that which would be obtained if the deflection of a beam of charged particles were measured instead.

Consider a particle of mass m and charge q with an initial trajectory perpendicular to a plane dipole strip passing near its edge. The geometry is shown in Fig. 24. The deflection angle α will be determined in an impulse approximation, with the deflection assumed to be small. If $\mathbf{F}=q\mathbf{E}$ is the force acting on the ion, with $\mathbf{E}$ given by Eqs. (4)–(6), then

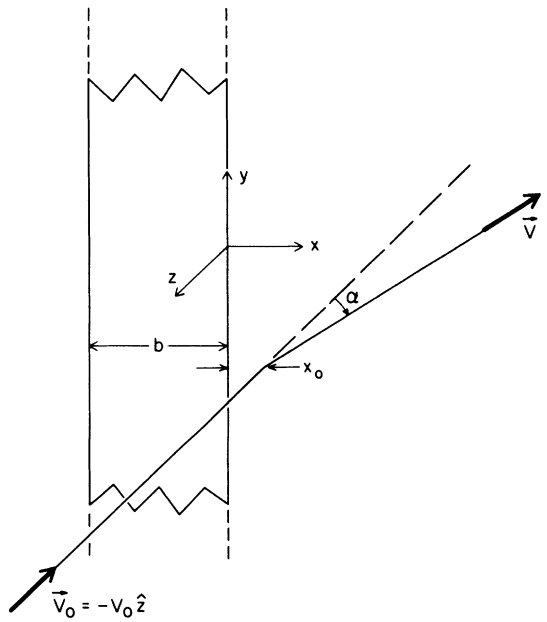

FIG. 24. Coordinates and geometry for a charged particle passing a uniformly covered dipole strip.

$$\alpha\cong\tan\alpha=\frac{v_x}{-v_z}\cong\frac{1}{v_0}\int_{-\infty}^{+\infty}dt\frac{F_x}{m}=\frac{q}{mv_0}\int_{+\infty}^{-\infty}\frac{dz}{v_z}E_x\ . \quad \text{(C1)}$$

The forward velocity component v_z and the transverse coordinate x (upon which E_x depends) are both weakly dependent on z in this approximation. They can be written in the form

$$v_z=-v_0-\eta(z) \quad \text{(C2)}$$

and

$$x=x_0+\xi(z)\ , \quad \text{(C3)}$$

where η and ξ are the small corrections to the initial values x_0 and v_0. An approximation for η is

$$-\eta\cong\frac{1}{m}\int_{-\infty}^{t}dt\,F_z\ , \quad \text{(C4)}$$

so that

$$\eta\cong-\frac{q}{m}\int_{\infty}^{z}\frac{dz}{v_z}E_z$$
$$\cong\frac{-q}{mv_0}\int_{\infty}^{z}dz\,2N\mu\left[\frac{x_0+b}{(x_0+b)^2+z^2}-\frac{x_0}{x_0^2+z^2}\right]$$
$$\cong\frac{-q}{mv_0}2N\mu\left[\tan^{-1}\left[\frac{(x_0+b)}{z}\right]-\tan^{-1}\left[\frac{x_0}{z}\right]\right]. \quad \text{(C5)}$$

To find ξ, first note that

$$v_x=v_z\frac{d\xi}{dz}\ , \quad \text{(C6)}$$

and approximate

$$v_x\cong\int_{-\infty}^{t}dt\frac{F_x}{m}=\frac{q}{m}\int_{\infty}^{z}\frac{dz}{v_z}E_x$$
$$\cong\frac{-q}{mv_0}\int_{\infty}^{z}dz\,2N\mu z\left[\frac{-1}{(x_0+b)^2+z^2}+\frac{1}{x_0^2+z^2}\right]$$
$$=\frac{qN\mu}{mv_0}\{\ln[(x_0+a)^2+z^2]-\ln(x_0^2+z^2)\}\ . \quad \text{(C7)}$$

Integration of Eq. (C7) yields

$$\xi=\int_{\infty}^{z}dz\frac{v_x}{v_z}$$
$$\cong\frac{-1}{v_0}\frac{qN\mu}{mv_0}\int_{\infty}^{z}dz\{\ln[(x_0+b)^2+z^2]-\ln(x_0^2+z^2)\}$$
$$=\frac{-qN\mu}{mv_0^2}\left[z\ln[(x_0+b)^2+z^2]-z\ln(x_0^2+z^2)+2(x+b)\tan^{-1}\left[\frac{z}{x_0+b}\right]-\pi b-2x_0\tan^{-1}\left[\frac{z}{x_0}\right]\right]. \quad \text{(C8)}$$

Return now to the deflection, keeping only the first-order corrections:

$$\frac{1}{v_z}=\frac{1}{-v_0-\eta}=-\frac{1}{v_0}\left[1+\frac{\eta}{v_0}\right]^{-1}\cong-\frac{1}{v_0}\left[1-\frac{\eta}{v_0}\right], \quad \text{(C9)}$$

$$E_x\cong E_{x0}+\xi\left[\frac{\partial E_x}{\partial x}\right]_0, \quad \text{(C10)}$$

$$\alpha\cong\frac{-q}{mv_0^2}\int_{+\infty}^{-\infty}dz\left[1-\frac{\eta}{v_0}\right]\left[E_{x0}+\xi\left[\frac{\partial E_x}{\partial x}\right]_0\right]$$
$$\cong\frac{-q}{mv_0^2}\int_{+\infty}^{-\infty}dz\left[E_{x0}-\frac{\eta}{v_0}E_{x0}+\xi\left[\frac{\partial E_x}{\partial x}\right]_0\right]. \quad \text{(C11)}$$

E_x is an odd function of z, so the first term integrates to zero, and the deflection is zero in lowest order. The second term can be evaluated as follows:

$$\frac{q}{mv_0^3}\int_{-\infty}^{\infty}dz\,\eta E_{x0}=\frac{q}{mv_0^3}\int_{-\infty}^{\infty}dz\left[\frac{-2qN\mu}{mv_0}\right]\left[\tan^{-1}\left[\frac{(x_0+b)}{z}\right]-\tan^{-1}\left[\frac{x_0}{z}\right]\right]2N\mu z\left[\frac{-1}{(x_0+b)^2}+\frac{1}{x_0^2+z^2}\right]. \quad \text{(C12)}$$

With the substitution $\zeta=1/z$, this becomes

$$\frac{q}{mv_0^3}\int_{-\infty}^{\infty}dz\,\eta E_{x0}=2\left[\frac{2qN\mu}{mv_0^2}\right]^2\int_0^{\infty}\frac{d\zeta}{\zeta}\left[\frac{\tan^{-1}[(x_0+b)\zeta]}{1+\zeta^2(x_0+b)^2}-\frac{\tan^{-1}[(x_0+b)\zeta]}{1+\zeta^2x_0^2}-\frac{\tan^{-1}(x_0\zeta)}{1+\zeta^2(x_0+b)^2}+\frac{\tan^{-1}(x_0\zeta)}{1+\zeta^2x_0^2}\right]$$
$$=\pi\left[\frac{2qN\mu}{mv_0^2}\right]^2\ln\left[\frac{4x_0(x_0+b)}{(2x_0+b)^2}\right]. \quad \text{(C13)}$$

The third and final term in the deflection, Eq. (C11), is

$$\frac{q}{mv_0^2}\int_{-\infty}^{\infty}dz\,\xi\left[\frac{\partial E_x}{\partial x}\right]_0=\frac{q}{mv_0^2}\int_{-\infty}^{\infty}dz\frac{-qN\mu}{mv_0^2}\left[z\ln[(x_0+b)^2+z^2]-z\ln(x_0^2+z^2)+2(x_0+b)\tan^{-1}\left[\frac{z}{x_0+b}\right]-\pi b-2x_0\tan^{-1}\left[\frac{z}{x_0}\right]\right]4N\mu z\left[\frac{x_0+b}{[(x_0+b)^2+z^2]^2}-\frac{x_0}{(x_0^2+z^2)^2}\right]. \quad \text{(C14)}$$

Of the ten integrals appearing when the multiplication is carried out in Eq. (C14), two are zero by symmetry and the remaining eight are available in tables. This term makes the same contribution to the deflection as the second term, namely,

$$\frac{q}{mv_0^3}\int_{-\infty}^{\infty}dz\,\xi\left[\frac{\partial E_x}{\partial x}\right]_0=-\pi\left[\frac{2qN\mu}{mv_0^2}\right]^2\ln\left[\frac{4x_0(x_0+b)}{(2x_0+b)^2}\right]. \quad \text{(C15)}$$

Equations (C11), (C13), and (C15) can be combined to give the deflection

$$\alpha=2\pi\left[\frac{2qN\mu}{mv_0^2}\right]^2\ln\left[\frac{(2x_0+b)^2}{4x_0(x_0+b)}\right]. \quad \text{(C16)}$$

As noted in Sec. III, the values for α tend to be quite small. This result follows from the vanishing of the first-order contribution and the short path length (10^{-3} to 10^{-4} cm) over which the electric field acts.

*Present address: Department of Physics and Engineering, Pacific Lutheran University, Tacoma, WA 98447.

[1]T. Engel and K. H. Rieder, in *Structural Studies of Surfaces*, Vol. 91 of *Springer Tracts in Modern Physics*, edited by G. Höhler (Springer-Verlag, Berlin, 1982), Chap. 2, pp. 55–180.

[2]A. Shih and V. A. Parsegian, Phys. Rev. A **12**, 835 (1975), and references therein.

[3]C. A. Kocher and C. R. Taylor, Phys. Lett. A **124**, 68 (1987).

[4]C. R. Taylor, Ph.D. thesis, Oregon State University, Corvallis, Oregon (1987).

[5]S. A. Edelstein and T. F. Gallagher, Adv. At. Mol. Phys. **14**, 365 (1978).

[6]H. Rinneberg, J. Neukammer, G. Jönsson, H. Hieronymus, A. König, and K. Vietzke, Phys. Rev. Lett. **55**, 382 (1985).
[7]T. H. Jeys, G. B. McMillian, K. A. Smith, F. B. Dunning, and R. F. Stebbings, Phys. Rev. A **26**, 335 (1982).
[8]A. V. Chaplik, Zh. Eksp. Teor. Fiz. **54**, 332 (1968) [Sov. Phys.—JETP **27**, 178 (1968)].
[9]R. K. Janev, J. Phys. B **7**, 1506 (1974); **7**, L359 (1974).
[10]C. Fabre, M. Gross, J. M. Raimond, and S. Haroche, J. Phys. B **16**, L671 (1983).
[11]J. D. Jackson, *Classical Electrodynamics,* 2nd ed. (Wiley, New York, 1975), Sec. 1.6.
[12]C. A. Kocher and A. J. Smith, Phys. Rev. Lett. **39**, 1516 (1977).
[13]C. R. Taylor and C. A. Kocher (unpublished).
[14]M. G. Littman, M. M. Kash, and D. Kleppner, Phys. Rev. Lett. **41**, 103 (1978).
[15]W. E. Cooke and T. F. Gallagher, Phys. Rev. A **21**, 588 (1980).
[16]C. A. Kocher and A. J. Smith, Phys. Lett. **61A**, 305 (1977).
[17]C. A. Kocher and C. L. Shepard, J. Chem. Phys. **74**, 379 (1981).
[18]N. F. Ramsey, *Molecular Beams* (Clarendon, Oxford, 1956), Chap. 2, Sec. 1.
[19]M. W. Roberts and C. S. McKee, *Chemistry of the Metal-Gas Interface* (Clarendon, Oxford, 1978), Sec. 12.4.
[20]J. P. Muscat and I. P. Batra, Phys. Rev. B **34**, 2889 (1986).
[21]J. E. Müller and J. Harris, Phys. Rev. Lett. **53**, 2493 (1984).
[22]R. L. Gerlach and T. N. Rhodin, Surf. Sci. **19**, 403 (1970).
[23]T. Takenaka, Y. Ito, and J. Oishi, Denki Kagaku Kogyo Butsuri Kagaku **53**, 476 (1985).